Published online 20 November 2018

Nucleic Acids Research, 2019, Vol. 47, No. 1 **15–28**
doi: 10.1093/nar/gky1110

Structure guided fluorescence labeling reveals a two-step binding mechanism of neomycin to its RNA aptamer

Henrik Gustmann [1], Anna-Lena J. Segler[2], Dnyaneshwar B. Gophane[2], Andreas J. Reuss[1], Christian Grünewald[3], Markus Braun[1], Julia E. Weigand [4], Snorri Th. Sigurdsson [2,*] and Josef Wachtveitl [1,*]

[1]Institute of Physical and Theoretical Chemistry, Goethe-University Frankfurt am Main, Max-von-Laue-Strasse 7, 60438 Frankfurt, Germany, [2]Science Institute, University of Iceland, Dunhaga 3, 107 Reykjavik, Iceland, [3]Institute for Organic Chemistry and Chemical Biology, Goethe-University Frankfurt am Main, Max-von-Laue-Strasse 7, 60438 Frankfurt, Germany and [4]Department of Biology, Technical University Darmstadt, Schnittspahnstraße 10, 64287 Darmstadt, Germany

Received July 26, 2018; Revised October 1, 2018; Editorial Decision October 20, 2018; Accepted October 22, 2018

ABSTRACT

The ability of the cytidine analog $Ç_m^f$ to act as a position specific reporter of RNA-dynamics was spectroscopically evaluated. $Ç_m^f$-labeled single- and double-stranded RNAs differ in their fluorescence lifetimes, quantum yields and anisotropies. These observables were also influenced by the nucleobases flanking $Ç_m^f$. This conformation and position specificity allowed to investigate the binding dynamics and mechanism of neomycin to its aptamer N1 by independently incorporating $Ç_m^f$ at four different positions within the aptamer. Remarkably fast binding kinetics of neomycin binding was observed with stopped-flow measurements, which could be satisfactorily explained with a two-step binding. Conformational selection was identified as the dominant mechanism.

INTRODUCTION

RNA is a ubiquitous biopolymer and essential to life. After the discovery of ribozymes in the laboratories of Altman (1) and Cech (2), the 'RNA world' hypothesis was put forth (3,4), in which RNA is the central biopolymer during the evolution of life, that both carries genetic information and catalyzes reactions. Since this hypothesis was proposed, many more roles of RNA, such as regulation of gene expression have been discovered (5,6). In particular, for gene regulation mediated by riboswitches (7–10), RNA motifs found in the 5′-untranslated regions of bacterial mRNAs (11) rely on binding to small molecules that induce conformational transitions in the RNA. The ligands bind to the aptamer region of the riboswitch and induce secondary structural changes (12,13) that determine the output of the expression platform (12,14). Central for the overall function is thus the aptamer, which binds the ligand with an extraordinary high affinity and specificity (15). It is therefore of great interest to study such binding motifs and to obtain a molecular picture of the mechanisms with which RNA binds its cognate ligand.

Prior to the discovery of riboswitches, RNA aptamers for a wide range of ligands have been found with the help of *in vitro* selection, using the technique of systematic evolution of ligands by exponential enrichment (SELEX) (16–18). One example is the 27 nucleotide **N1** neomycin-sensing aptamer, one of the smallest known aptamers (Figure 1A and C) (13) that binds with high affinity ($K_d = 10 \pm 2.0$ nM) to the aminoglycoside antibiotic neomycin (Figure 1B) (19). The aptamer consists of a closing stem as well as an internal loop and a terminal loop that are connected by a short helical stem region. Nuclear magnetic resonance (NMR) studies have revealed that the binding pocket of the aptamer is formed by the internal and the terminal loop, in which the two helical stems form a continuous A-form helix with stacking between G5:C23 and G9:C22 (Figure 1A and C) (19,20). The A-form helix is intersected by a bulging internal loop (C6, U7, U8) that together form the binding pocket with A17 of the terminal loop (19). NMR and electron paramagnetic resonance (EPR) spectroscopic studies have shown that the binding pocket is preformed and that neomycin is bound to the aptamer via a conformational selection mechanism (19–21). When bound, ring I and ring II of neomycin are clamped between G5:C23 and U13:U18 of the aptamer (Figure 1) while forming hydrogen bonds to G9

*To whom correspondence should be addressed. Tel: +49 069 798 29351; Fax: +49 069 798 29709; Email: wveitl@theochem.uni-frankfurt.de
Correspondence may also be addressed to Snorri Th. Sigurdsson. Tel: +354 525 4801; Email: snorrisi@hi.is

and U10, in addition to electrostatic interactions to G9 and A17 (19).

Structural information is indispensable for understanding RNA–ligand recognition. However, the mechanistic picture is not complete without information on the dynamics of the aptamer. Optical spectroscopy is a valuable technique to obtain information about motion on all time scales relevant for molecular dynamics, from fs to minutes. Although UV/vis spectroscopy can be useful for this purpose, the absorption changes upon ligand binding to RNA are typically rather unspecific. In contrast, fluorescence spectroscopic values like quantum yield, lifetime or anisotropy allow deeper insights of micro-environment changes upon ligand binding at a defined position within the RNA. However, fluorescence studies require reporter labels since neither RNA nor most ligands are fluorescent (22). Fluorescent labels have to meet several requirements, depending on the application. In particular, it should be possible to incorporate them site-specifically. In addition, they should be non-perturbing, highly fluorescent and should not absorb in the same spectral region as the RNA or the ligands. For RNA and DNA, 2-aminopurine is perhaps the most widely used fluorescent label (23–26). Furthermore, several other fluorescent base analogs have been developed and characterized in the last years (26–40). For example there are many pyrene- (28–32), phenothiazine- (34), isothiazole- (33) and phenylpyrrole-derivatives (36) of nucleic acid bases.

A very valuable feature of spectroscopic labels is multifunctionality, where the same label can be used for different spectroscopic methods that give complementary information. One paragon is **Ç** (41), a cytidine analog that is successfully used as rigid spin label for DNA. Pulsed electron-electron double resonance (PELDOR, sometimes called DEER) experiments can determine precise distances between two spin labels, as well as information about their relative orientation (41–50). Reduction of the nitroxide in **Ç** with a mild reducing agent yields a strongly fluorescent nucleoside (41). Thus, the nitroxide acts as an efficient fluorescence quencher (51–53). The fluorescent and isosteric $\mathbf{Ç^f}$ is the direct synthetic precursor of **Ç**. Therefore, it can be used as a rigid, non-perturbing fluorescent probe for steady-state and time-resolved fluorescence studies of nucleic acids (41,43,46,54–56). The structural similarity of both labels makes the results of EPR and fluorescence studies highly comparable (42,43,46,47,50,54–56). More recently, we have prepared the analogous nucleoside label $\mathbf{Ç_m}$ (45), containing a 2′-methoxy group (Figure 2) and established as a label for EPR studies of RNA (45,57). However, $\mathbf{Ç_m^f}$ has not yet been used as a fluorescent label in RNA. Here, we present a detailed characterization of $\mathbf{Ç_m^f}$ as a fluorescent label for both steady-state and time-resolved fluorescence measurements in RNA single-strands and duplexes. In the discussion, we compare our results on $\mathbf{Ç_m^f}$ with the photophysical properties of tC°. tC° is a recently well characterized fluorescent cytosine analog by the Wilhelmsson group which shows high structural as well as photophysical similarity to $\mathbf{Ç_m^f}$ (58). Furthermore, we have incorporated $\mathbf{Ç_m^f}$ into the neomycin aptamer and investigated the change in fluorescence upon ligand binding, including fast-binding kinetics using stopped-flow measurements. Our results can be explained by a two-step binding mechanism of neomycin to its aptamer.

MATERIALS AND METHODS

Preparation of oligonucleotides

The benchmark non-selfcomplementary oligoribonucleotide (29) that was used for characterization of $\mathbf{Ç_m^f}$ contained the $\mathbf{Ç_m^f}$ label in the center of a 15-mer (5′-UAC-GCA-N$\mathbf{Ç_m^f}$N-ACG-CAU-3′). An unlabeled 15-mer complementary to this sequence (3′-AUG-CGU-N′GN′-UGC-GUA-5′) was annealed to form the corresponding duplex. To study flanking sequence effects on the $\mathbf{Ç_m^f}$ signal, the bases immediately flanking the label (N in the strand and N′ in the counter-strand) were permuted such that for each oligomer the $\mathbf{Ç_m^f}$ was flanked on both sides with either A, C, G or U, to yield four duplexes (Supplementary Table S1). The corresponding unlabeled RNA duplexes were also prepared for comparison in the thermal denaturation experiments (see below).

The neomycin aptamer (5′-GGC-UGC-UUG-UCC-UUU-AAU-GGU-CCA-GUC-3′) was singly labeled with $\mathbf{Ç_m^f}$ at the positions 6, 8, 15 and 22 (Table 1).

The synthesis of the $\mathbf{Ç_m^f}$-labeled benchmark oligoribonucleotides as well as the synthesis of the $\mathbf{Ç_m^f}$-labeled neomycin aptamers are described in the Supplementary Data.

Sample preparation

The RNA model sequences were dissolved in 20 mM sodium cacodylate buffer with pH 7.4. This buffer was chosen, because the pH-value of sodium cacodylate buffer is not temperature dependent, which is essential for the melting studies (59). All experiments were carried out with a 7 μM RNA model strand solution. The neomycin aptamer samples were dissolved in 20 mM sodium cacodylate and 100 mM NaCl buffer at pH 7.4. All steady-state experiments of the aptamer samples were carried out with a 1 μM aptamer (without neomycin; **−Neo**) solution. Neomycin was added in excess (4 μM neomycin; **+ Neo**). Before each series of measurements, the samples (model strands and aptamers) were annealed. The samples were heated up to 90°C for 2 min and left to cool down to room temperature.

Steady-state spectroscopy

Steady-state absorption spectra were recorded in 10 × 4 mm UV-grade quartz cuvettes (29-F/Q/10, Starna GmbH, Pfungstadt, Germany) on a JASCO V-650 spectrometer (JASCO Germany GmbH, Groß-Umstadt, Germany). The spectra were offset corrected and normalized. Emission spectra were recorded in 10 × 4 mm UV-grade quartz cuvettes (29-F/Q/10, Starna GmbH) with a JASCO FP 8500 fluorescence spectrometer. Prior to normalization, the spectra were corrected for offset, absorption and reabsorption artifacts as well as the spectral characteristics of the experimental equipment. The JASCO FP 8500 spectrometer was equipped with a 100 mm integrating sphere (ILF-835, JASCO) and used for absolute fluorescence quantum yield

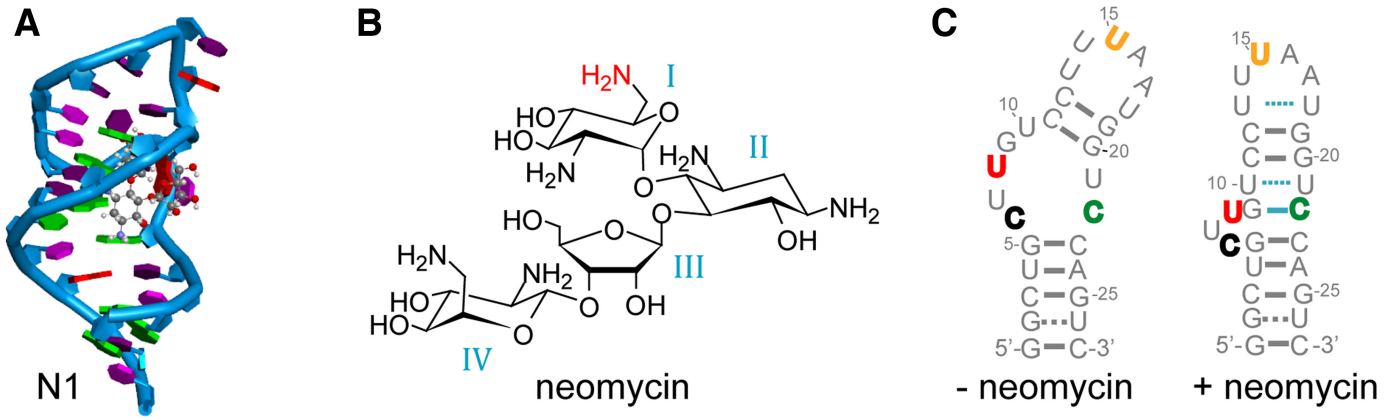

Figure 1. (**A**) NMR structure (NDB/PDB-ID: 2KXM) of the **N1** neomycin aptamer with bound ligand (here ribostamycin) (20). (**B**) Structure of neomycin B. The NH_2-group marked in red, protonated at physiological pH, contributes to the H-bonding pattern of the neomycin aptamer (19). (**C**) Predicted structures of the ligand unbound (left) and bound (right) state of the neomycin aptamer (19,20). Bold-colored letters mark the different **Ç$_m$^{f}** labeling positions.

Table 1. Sequences of the **Ç$_m$^{f}**-labeled neomycin aptamer samples

Sample	Sequences
Ç$_m$^{f}6	5′-GGC-UG**Ç$_m$^{f}**-UUG-UCC-UUU-AAU-GGU-CCA-GUC-3′
Ç$_m$^{f}8	5′-GGC-UGC-U**Ç$_m$^{f}**G-UCC-UUU-AAU-GGU-CCA-GUC-3′
Ç$_m$^{f}15	5′-GGC-UGC-UUG-UCC-UU**Ç$_m$^{f}**-AAU-GGU-CCA-GUC-3′
Ç$_m$^{f}22	5′-GGC-UGC-UUG-UCC-UUU-AAU-GGU-**Ç$_m$^{f}**CA-GUC-3′

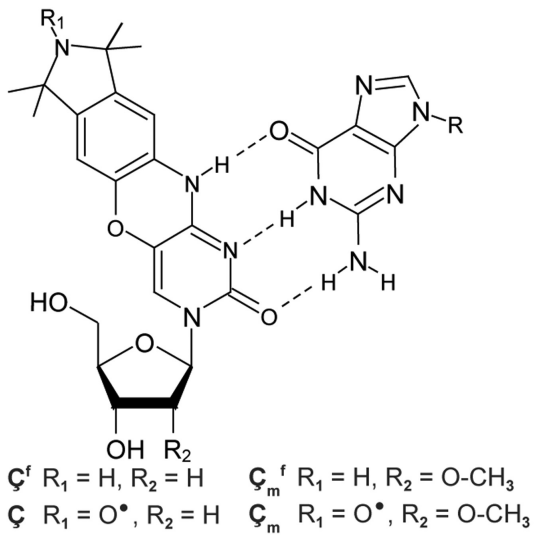

Figure 2. **Ç**, **Ç^f**, **Ç$_m$** and **Ç$_m$^{f}** base paired with guanine.

(QY) determinations. For anisotropy studies, the spectrometer was equipped additionally with two automatized polarization filters as polarizer and analyzer (FDP-837, JASCO).

Thermal denaturation experiments

For the melting analyses, the absorption changes of the RNA band at 260 nm was recorded from 20°C to 90°C. The change of the **Ç$_m$^{f}** emission around 460 nm upon excitation of the label at 360 nm, was also recorded in the same temperature range. The full absorption as well as the emission spectra were recorded at 5°C intervals (Supplementary Figures S6 and 8). Thus, it was possible to detect changes of the spectral position and shape of the observed signal bands. To determine the melting temperatures and the thermodynamic parameters, the signal changes at single wavelengths were recorded every 0.5°C. The temperature was changed between the single measuring points with a rate of 1°C/min. The heating and cooling curves were averaged to compensate for possible hysteresis effects. For the determination of the melting temperatures and the thermodynamic parameters, the method described by Mergny and Lacroix was used (Supplementary Figure S7) (59). A slope correction that accounts for the increase of collisional quenching with temperature was performed for the emission data recorded around 460 nm (cf. Supplementary Figure S9 and Table S4), but this procedure did not affect the determined melting point significantly.

Isothermal titration calorimetry

For isothermal titration calorimetry (ITC) experiments, an iTC200 microcalorimeter (MicroCal, GE Healthcare, Buckinghamshire, UK) was used. The sample cell of the iTC200 was filled with the RNA sample (10 μM RNA, 20 mM sodium cacodylate, 200 mM NaCl, pH 7.4). The injector syringe was filled with a neomycin solution (75 μM neomycin, 20 mM sodium cacodylate, 200 mM NaCl, pH 7.4). After equilibrating the system at 20°C for 10 min, the measurements were started with an initial 120 s delay and a 0.2 μl injection. Subsequently 20 injections of 2.0 μl at a 180 s interval were made. The sample cell was stirred with a speed of 750 rpm (60). The software NITPIC was used to integrate the injection peaks to yield the associated heat for

each injection (61,62), the experimental binding isotherm was subsequently plotted and the curve fit with a one-site binding model using the software SEDPHAT (63). This fit made it possible to determine the dissociation constant (K_D).

Time-resolved fluorescence

The fluorescence lifetimes were measured with a partially home-built time-correlated single photon counting (TCSPC) setup as previously described (40). For excitation, a mode-locked titanium-doped sapphire (Ti:Sa) laser (Tsunami 3941-X3BB, Spectra-Physics, Darmstadt, Germany) was pumped by a 10 W continuous wave diode pumped solid state laser (Millennia eV, Spectra-Physics, 532 nm). The Ti:Sa laser provided pulses of 775 nm central wavelength with a repetition rate of 80 MHz. With the help of an acousto-optic modulator, the repetition rate was reduced to 8 MHz and the excitation wavelength of 388 nm was obtained by SHG in a BBO crystal (frequency doubler and pulse selector, Model 3980, Spectra-Physics). Excitation pulses of about 0.1 nJ at 388 nm were applied to the sample. The sample was prepared in a 10 × 4 mm quartz cuvette (29-F/Q/10, Starna) with a fixed temperature of 20°C. Emission filters (GG395, GG400, Schott AG, Mainz, Germany) suppressed excitation stray light. The instrument response function (IRF, FWHM 200 ps) was obtained without emission filters using a TiO_2 suspension as scattering sample. For single-photon detection, a photomultiplier tube (PMT, PMA-C 182-M, PicoQuant, Berlin, Germany) and a TimeHarp 260 PICO Single PCIe card (PicoQuant) were used. Multi-exponential fitting was carried out with FluoFit Pro 4.6 (PicoQuant) (64).

Fluorescence stopped-flow

Mixing experiments were performed with a SFM-20 stopped-flow setup (65) (Bio-Logic Science Instruments, Seyssinet-Pariset, France) using a Berger ball mixer (66) and cuvette (FC08) with an approximate volume of 20 μl and a light path of 0.8 mm. The mixing was controlled and triggered by a Microprocessor unit (MPS-60, Bio-Logic), which was driven by the Bio-Kine 32 software (Version 4.42, Bio-Logic Science Instruments). For each mixing experiment, two sample solutions (volume: each 33 μl) were injected in the Berger ball mixer via two syringes (Hamilton 1010C, Hamilton Company, Reno, USA) for 9.5 ms, resulting in a flow rate of 6.95 ml/s. The injection was stopped by a hard-stop valve. For excitation and detection, the stopped-flow setup was fiber-coupled (OBF-832, JASCO) with a JASCO FP 8500 fluorescence spectrometer. The sample was excited with 360 nm light and the resulting fluorescence at 460 nm was measured under an angle of 90° with the PMT-detector of the FP 8500. With the help of an A/D-adapter (BNC-2110, National Instruments, Austin, USA) the PMT-signal was transferred to a transient recorder board (PCI-6052E, National Instruments). Data acquisition was controlled by the Bio-Kine 32 software. The transients were digitized with 6000 equidistant points of 10 μs.

For ligand-concentration dependence studies, a fluorescent-labeled aptamer solution (**$Ç_m^f$6**: 2.7 μM, **$Ç_m^f$8**: 4 μM) was mixed with ligand solutions of 8 different concentrations (0, 2, 4, 8, 16, 24, 32, 40 μM). For each concentration, at least 20 single mixing transients were averaged. Prior to fitting of all transients, the offset was corrected (subtraction of the fluorescence signal of unbound labeled aptamer) and the start point of the dynamic analysis was set to the end of the mixing, which is given by the hard stop. The corrected set of transients was processed using the Dynafit software (Biokin Ltd., Watertown, USA) to test different reaction models and to derive the reaction constants for the best model (67).

RESULTS

Photophysical properties of $Ç_m^f$ in single- and double-stranded RNA

Steady-state spectra and quantum yields. Steady-state fluorescence measurements of the singly **$Ç_m^f$**-labeled double-strands (ds) and single-strands (ss) are shown in Figure 3 (Supplementary Figure S8). Both the four spectra of the single- and the double strands are similar to each other, but the two sets of double- and single-strand spectra show pronounced spectral differences with respect to each other. Specifically, the emission spectra of the duplexes show a vibrational fine structure with maxima at 420, 448, 480 and 520 nm, which has already been described for **$Ç^f$** in DNA and was used for mismatch detection (54). The fluorescence spectrum of ds-C**$Ç_m^f$**C is slightly blue-shifted in comparison to the other spectra of the double-strands. Thus, double- and single-strands can be spectrally distinguished based on the fine structure of the spectra of the double-strands.

As might be expected, the double- and single-stranded RNAs differ significantly in their fluorescence quantum yields (QY, Table 2). While the ds RNAs show an average quantum yield (QY_{av}) of 24%, the single-strands show a QY_{av} of 44%. In comparison to the fluorophore itself (QY = 38%) (68), QY decreases upon incorporation into double-stranded RNA but increases upon incorporation into single-stranded RNA. The QYs of the double-stranded RNAs are affected by the flanking nucleobases: the QYs are slightly higher for the purines.

Fluorescence anisotropy. The steady-state fluorescence anisotropy (r_f) of the **$Ç_m^f$**-labeled double- and single-stranded RNA is significantly higher than the anisotropy of the fluorophore itself in solution. This confirms that the motion of the label is restricted after incorporation into the RNA. Additionally, the anisotropy of the double-stranded RNA is systematically higher (by a factor 1.4) than the anisotropy of the single-strands (Table 2), which is consistent with a greater order of the more rigid duplex. The anisotropy values for the samples with purine bases adjacent to the fluorophore site are slightly lower than for the samples with adjacent pyrimidine bases.

Thermal denaturation. To determine the effect of **$Ç_m^f$** on duplex stability, which would indicate possible structural perturbations, thermal denaturation experiments were performed on both labeled and unlabeled RNA duplexes, by

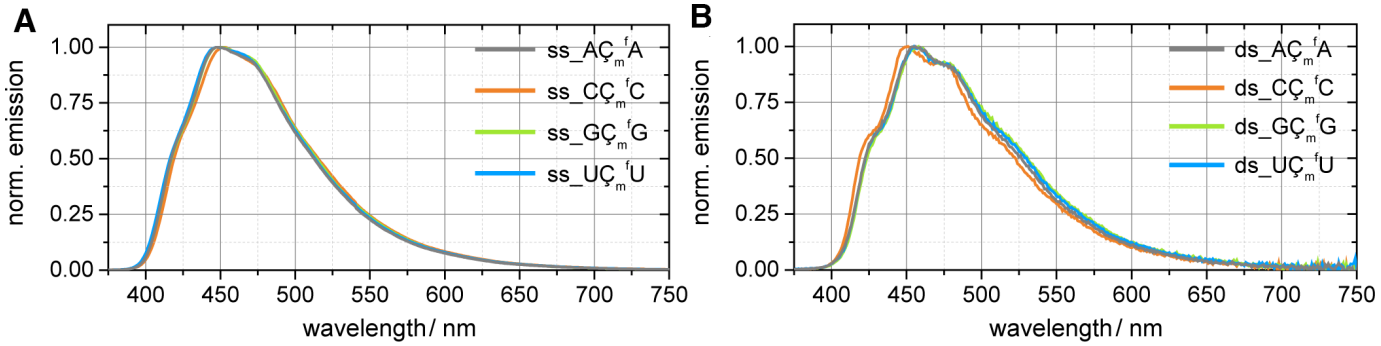

Figure 3. Normalized emission spectra of **Çm^f**-labeled (**A**) single-stranded and (**B**) double-stranded RNA at 20°C.

Table 2. Fluorescence lifetime (τ), quantum yield (QY) and steady-state anisotropy (r_f) of Çm^f labeled single- (ss) and double-stranded (ds) RNA at 20°C

	Sample	τ_{pop}/ns	τ_1/ns	τ_2/ns	χ^2	τ_{av}/ns	QY/%	r_f
	Çm^f	0.3	4.1 (96%)	1.4 (4%)	1.1	4.1	38	0.04
ds	**AÇm^{f}A**	1.5	4.6 (89%)	7.6 (11%)	1.2	5.3	25	0.12
	CÇm^{f}C	1.7	4.1 (96%)	6.8 (4%)	1.1	4.5	22	0.14
	GÇm^{f}G	2.3	4.7 (97%)	7.5 (3%)	1.3	5.2	26	0.14
	UÇm^{f}U	1.6	4.2 (97%)	7.4 (3%)	1.1	4.6	22	0.17
ss	**AÇm^{f}A**	1.5	6.4 (71%)	8.5 (29%)	1.1	7.5	54	0.08
	CÇm^{f}C	1.5	5.1 (77%)	8.2 (23%)	1.1	6.4	39	0.11
	GÇm^{f}G	1.6	5.6 (69%)	8.2 (31%)	1.1	7	42	0.09
	UÇm^{f}U	1.9	3.9 (36%)	6.8 (64%)	1.2	6.5	41	0.09

τ_{pop} = lifetime with a negative amplitude, representing the population of a fluorescent state. τ_n = lifetime with a positive amplitude, representing the depopulation of a fluorescent state. τ_{av} = average fluorescence lifetime. X^2 = reduced chi-square value, as measure of the quality of the fit (cf. Supplementary Data).

monitoring both steady-state RNA absorption (at 260 nm) and **Çm^f** fluorescence (Table 3). The melting temperatures recorded by the two methods (T_{m_abs} and T_{m_em}) are very similar, which indicates a homogeneous melting behavior of the labeled RNA duplex. The difference of only −1 to 3°C in T_m between unlabeled and labeled RNA duplexes provides evidence for a negligible effect of the label on duplex stability. The melting temperatures of C**Çm^f**C and G**Çm^f**G were higher than the melting temperatures of A**Çm^f**A and U**Çm^f**U, presumably because of the higher CG-content of the former. Table 3 also shows the free enthalpies (ΔG) that were determined from the melting data obtained from the 260 nm absorption.

The fluorescence signal of the single-stranded RNA decreased with increasing temperature (Figure 4A). This may be due to enhanced quenching through an increased flexibility of the strands, which in turn could lead to higher collision rates due to less steric shielding. For ss_A**Çm^f**A, ss_C**Çm^f**C and ss_U**Çm^f**U this led to a strong quenching, while ss_G**Çm^f**G was only slightly affected. The latter effect may be due to stacking effects around the label. Interestingly, in case of pyrimidines flanking the label (ss_U**Çm^f**U and ss_C**Çm^f**C), a slight emission increase between 20°C and 50°C is notable. This might be due to conformational changes, which increase the solvent shielding of **Çm^f** and as a consequence the QY in this temperature region.

The fluorescence-monitored melting curves of the RNA duplexes show a very different behavior (Figure 4B). Initially, the emission decreased with increasing temperature. Subsequently, a steep and strong increase of the emission was observed due to the melting of the RNA duplexes and thereby an increase of unpaired RNA strands. After melting of the RNA duplexes, the fluorescence intensity decreased, most likely due to collisional quenching.

The fine structure of the emission spectra of the duplexes disappeared upon heating (Supplementary Figure S8). This effect can be used for further analysis of the melting process: The emission spectrum of a sample at 20°C should represent a nearly 100% double-stranded RNA, while in a first approximation the emission spectrum with the highest QY should stem from a nearly 100% single-stranded RNA. Furthermore, we assume the decay of the fine structure to be linear with temperature. Under these assumptions, it is possible to reconstruct all normalized emission spectra based on a certain ratio of these two spectral extremes (Figure 5). A MATLAB script (Supplementary Data) was used to perform a nonlinear least-squares fitting of the spectra. This method, which we refer to as a spectrally resolved melting analysis, yielded a decrease of the double stranded RNA content as a function of increasing temperature (Figure 5B). Thus, the temperature which shows apparently 50% double stranded RNA can be interpreted as the melting temperature (T_{m_sr}), which is 14–22°C lower than the melting temperatures determined by the conventional melting analyses. One plausible explanation for this deviation is that T_{m_sr} reflects the breaking of the Watson–Crick hydrogen-bonds of **Çm^f** and thus the very first step of the (local) melting process. This is followed by the separation of the two complemen-

Table 3. Melting temperatures and thermodynamic parameters of the unlabeled and labeled RNAs

	Unlabeled		Ç$_m$^{f} -labeled					
Sample	T_{m_abs}/°C	-ΔG_{abs} (37°C)/ kcal/mol	T_{m_abs}/°C	T_{m_em}/°C	T_{m_sr}/°C	-ΔG_{abs} (37°C)/ kcal/mol	ΔT_{m_abs}/°C	$\Delta\Delta G_{abs}$ (37°C)/kcal/mol
AÇ$_m$^{f}A	70	18	67	67	45	13	3	−5
CÇ$_m$^{f}C	81	20	82	81	63	15	−1	−5
GÇ$_m$^{f}G	78	18	76	76	56	14	2	−4
UÇ$_m$^{f}U	70	17	72	70	56	15	−2	−2

T_{m_abs} = absorption monitored melting temperature; T_{m_em} = emission monitored melting temperature; T_{m_sr} = spectrally resolved melting analysis; $\Delta T_{m\_abs} = T_{m\_abs}$ (unlabeled) – T_{m_abs} (labeled); ΔG_{abs} = determined via melting analysis; $\Delta\Delta G_{abs} = \Delta G_{abs}$ (unlabeled) – ΔG_{abs} (labeled).

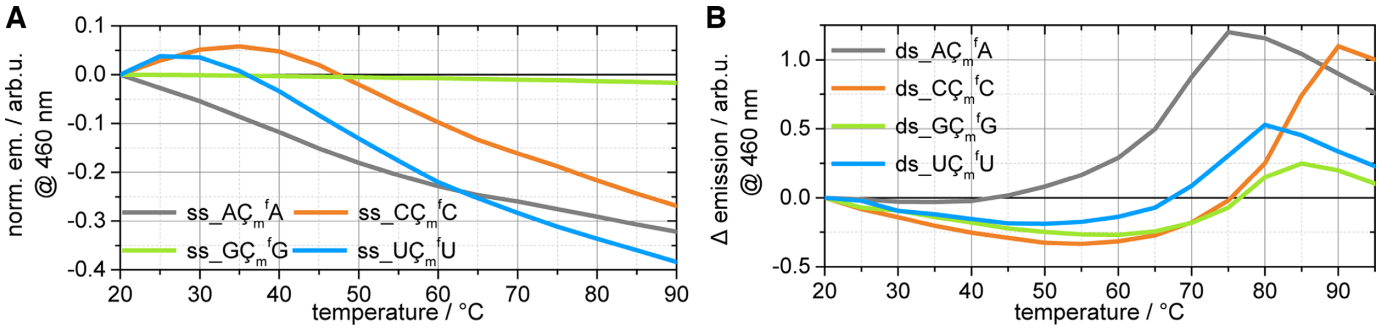

Figure 4. Fluorescence monitored melting curves of **Ç$_m$^{f}**-labeled (**A**) single-strands and (**B**) double-strands at 460 nm. All curves were set to zero at 20°C.

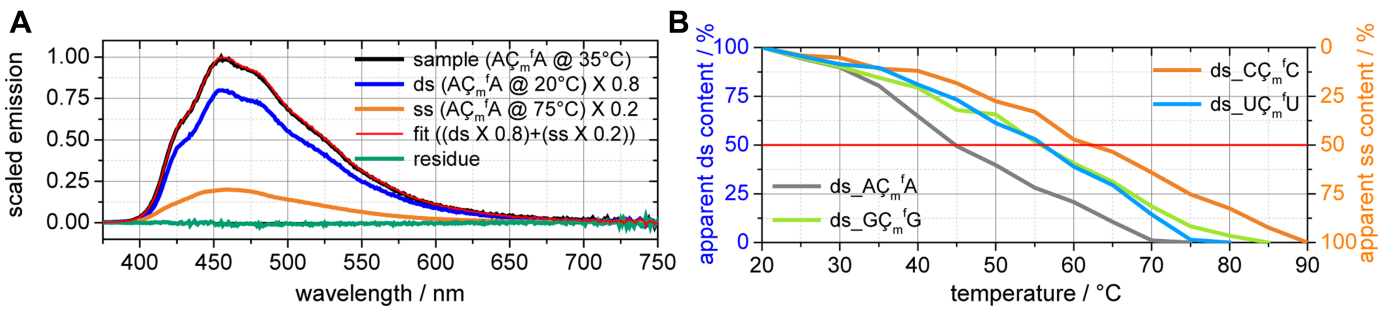

Figure 5. (**A**) Spectrally resolved melting analysis of the emission spectra of ds_AÇ$_m$^{f}A at 35°C. (**B**) Temperature dependence of the double-to-single-stranded-content of the four labeled double-stranded samples, determined by spectrally resolved melting analysis.

tary strands at a higher temperature (T_{m_abs}, T_{m_em}). Thus, the spectrally resolved melting analysis can be used for local probing of the melting process.

Fluorescence lifetime. The fluorescence lifetime (Figure 6) of **Ç$_m$^{f}** increased upon incorporation into either RNA single-strands or duplexes. Furthermore, the fluorescence lifetime of the single-strands was noticeably longer than that of the duplexes. It is also worth noting that the fluorescence lifetimes of the RNA where the label was flanked by pyrimidines (CÇ$_m$^{f}C and UÇ$_m$^{f}U) were shorter than for flanking purines (AÇ$_m$^{f}A and GÇ$_m$^{f}G) (Table 2). Specifically, the order observed was CÇ$_m$^{f}C < UÇ$_m$^{f}U < GÇ$_m$^{f}G < AÇ$_m$^{f}A. Hence, it is possible to use fluorescence lifetimes to distinguish between **Ç$_m$^{f}**-labeled single and double-stranded RNA and between neighboring purine and pyrimidine bases within this set of samples.

To describe the fluorescence decays satisfactorily, at least three exponential decay components were needed (Table 2). As we have previously shown, the fluorescence decay of **Ç$_m$^{f}** in an aqueous solution can be described by a short component of 0.3 ns (τ_{pop}, negative amplitude), which represents the population of the emitting state; the actual decay was fitted by two longer lifetimes (τ_1 = 4.1 ns and τ_2 = 1.4 ns) (68). As alluded to above, all the decay components of **Ç$_m$^{f}** in RNA are significantly prolonged, whereby the single-stranded RNA decay components are longer than those for double-stranded RNA by a factor of ca. 1.4. Notably, the amplitude of τ_2 is stronger for the single-strands than for the double-strands. With the help of temperature-dependent TCSPC measurements (Supplementary Figures S11–13 and Tables S8–15), it was possible to assign τ_2 to the amount of single-strands in the sample (Table 2).

Ç$_m$^{f}-labeled neomycin aptamers

Selection of labeling positions. For the fluorescently-labeled neomycin aptamer, four labeling positions were selected based on the NMR structure and the proposed binding model (19, 20): the cytidines or uridines at positions C6,

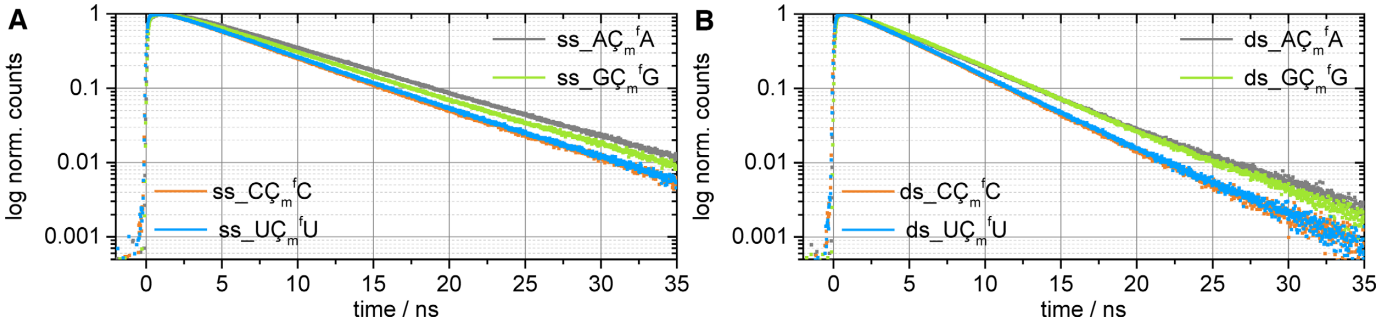

Figure 6. Normalized fluorescence decays of $Ç_m^f$ labeled (**A**) single- and (**B**) double stranded RNAs.

U8, U15 and C22 were exchanged with $Ç_m^f$ (Figures 1C and 7). Positions C6, U8 and U15 are located on both sides of the binding pocket and were chosen to avoid interference of the label with the binding event. Previous mutational analyses have shown that nucleotides at positions 6, 8 and 15 can be replaced by any nucleotide without loss of regulatory activity *in vivo* (60,69).

U15 and C22 should serve as reference or negative control samples: For $Ç_m^f$ at position C22 we expected major interference (steric hindrance) between the label and the ligand. For $Ç_m^f$ at the remote position U15, on the other hand, we did not expect any pronounced sensitivity for ligand binding or RNA conformational changes. All the RNAs were synthesized via solid phase chemical synthesis (See Supplementary Data).

ITC was performed to test the binding affinity of the $Ç_m^f$-labeled aptamers. As can be seen in Table 4, the K_D values of aptamers **$Ç_m^f$6**, **$Ç_m^f$8** and **$Ç_m^f$15** are 50- to 80-fold higher than the unlabeled aptamer. The K_D thus corresponds to the binding of the ligand ribostamycin to the wild-type (K_D 330 nM) (19). Ribostamycin binding to the neomycin aptamer is analogous to that of neomycin and accordingly shows regulatory activity *in vivo* (20). Thus, although significantly increased, the measured K_D values of **$Ç_m^f$6**, **$Ç_m^f$8** and **$Ç_m^f$15** are within a physiologically relevant range. In contrast, the ca. 2000-fold lower binding affinity of **$Ç_m^f$22** shows that there is effectively no ligand binding, as expected.

$Ç_m^f$15 should not sterically interfere with ligand binding. However, it is not unlikely that electrostatic repulsion increases the K_D for any of the labeling positions. It therefore can be assumed that the binding affinity at position 15 is reduced mainly by electrostatic effects. In addition, it has been shown that mutations at position 15 modulate the preformation of the terminal loop (60). Thus, although they do not alter ligand interactions within the binding pocket, mutations at this position can reduce binding affinity by affecting conformational selection.

Steady-state fluorescence. The emission spectra of the $Ç_m^f$ labeled aptamers (Figure 8) are quite similar to each other and to the free chromophore in solution (68). The unstructured spectra span from ca. 400 to 650 nm with a maximum at 460 nm. The only exception is the spectrum of **$Ç_m^f$22**, both in the presence and absence of neomycin. This spectrum shows the typical vibrational fine structure for a base-paired $Ç_m^f$, as described above. Upon addition of neomycin, the following effects were observed (Figure 8 and Table 4): The QYs of **$Ç_m^f$6** (+25%) and **$Ç_m^f$8** (+43%) increase significantly, while there is no significant (+4%) change for **$Ç_m^f$15** and even a slight decrease for **$Ç_m^f$22** (−10%).

Steady-state fluorescence anisotropy studies showed only slight differences for the four labeling positions (Table 4). Furthermore, the presence of the ligand does not have any significant effect on the anisotropy. However, the fluorescence anisotropy of **$Ç_m^f$22** is slightly higher than the fluorescence anisotropy of the other samples, presumably due to the expected misfolding of **$Ç_m^f$22**. This is independent of the presence of the neomycin ligand.

Thermal denaturation. Thermal denaturation was monitored by either absorption at 260 nm or by fluorescence at 460 nm. The thermal denaturation curves of the labeled and unlabeled aptamer samples as a function of absorbance show that $Ç_m^f$ only has a minor effect on the melting temperature (Table 4). Upon addition of neomycin, T_m increases for most of the samples. For the unlabeled aptamer, the increase was 10°C, while for **$Ç_m^f$6**, **$Ç_m^f$8** and **$Ç_m^f$15** the increase was 5–7°C. A decrease of the melting temperature of 2°C was observed for **$Ç_m^f$22**, further showing that a label in position 22 interferes with folding of the aptamer.

The results of fluorescence-monitored thermal denaturation experiments (Figure 9 and Table 4) differ from the absorption-monitored experiments. This was expected, since the $Ç_m^f$ is a site-specific probe for the local RNA melting. In the case of **$Ç_m^f$6**, **$Ç_m^f$8** and **$Ç_m^f$15**, the emission intensity generally decreases with rising temperature, due to collisional quenching. Without the ligand, the melting of the aptamer can be observed as a small increase in emission, which reduces the effect of the collisional quenching on the signal. Thus, this leads to a plateau-like range within the melting curve. In the presence of the ligand, the melting of the **$Ç_m^f$6** and **$Ç_m^f$8** aptamers can be observed as a region of a more pronounced signal decrease, while for **$Ç_m^f$15** the effect of neomycin is only very weak. The melting curve of **$Ç_m^f$22**, with and without neomycin, shows the typical sigmoidal shape for an RNA duplex.

As described above, the fluorescence signal is influenced by several parallel processes during the thermal denaturation experiments. Thus, the information density of these experiments is principally quite high. On the other hand, this complicates the analysis of these processes, especially in direct comparison with absorption monitored thermal denaturation experiments. Therefore, because of possible com-

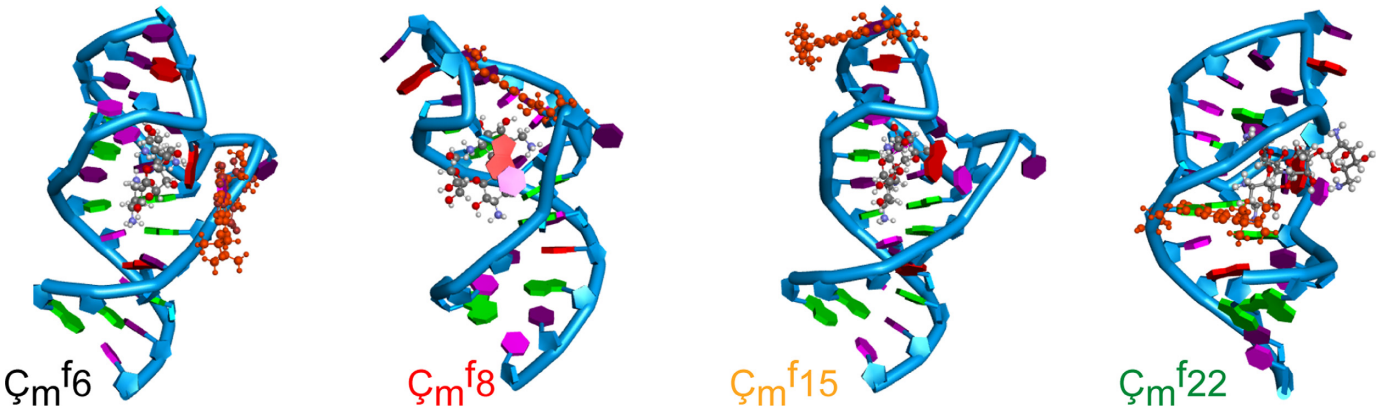

Figure 7. Positions of **Çm^f**-labeling within the neomycin aptamer (20), outlined in PDB ID: 2KXM (NDB/PDB). **Çm^f** (orange) is highlighted in ball-and-stick representation.

Table 4. Spectral shape (np/p), change of fluorescence quantum yield (ΔQY), average fluorescence lifetime (τ_{av}), steady-state fluorescence anisotropy (r_f), melting temperature (determined via absorption at 260 nm or emission at 460 nm) and K_D for different **Çm^f** labeled and unlabeled neomycin aptamers (**N1**) without (−**Neo**) and with neomycin (+**Neo**)

Sample	Neo	np/p	ΔQY/%	τ_{av}/ns	r_f	T_{m-em}/°C	T_{m-ab}/°C	K_D/nM
N1	–						56	6
	+						66	
Çm^{f}6	–	np		5.4	0.15	46 [+]	50	375
	+	np	+25	5.9	0.14	50 [–]	55	
Çm^{f}8	–	np		5.0	0.16	50 [+]	56	318
	+	np	+43	4.5	0.15	51 [–]	61	
Çm^{f}15	–	np		5.5	0.14	59 [+]	54	480
	+	np	+4	5.8	0.15	57 [–]	61	
Çm^{f}22	–	p		4.6	0.17	59 [+]	57	11 700
	+	p	−10	4.4	0.17	59 [+]	55	

np = not paired, p = paired; [–]/[+] indicating the trend of the ΔQY upon melting.

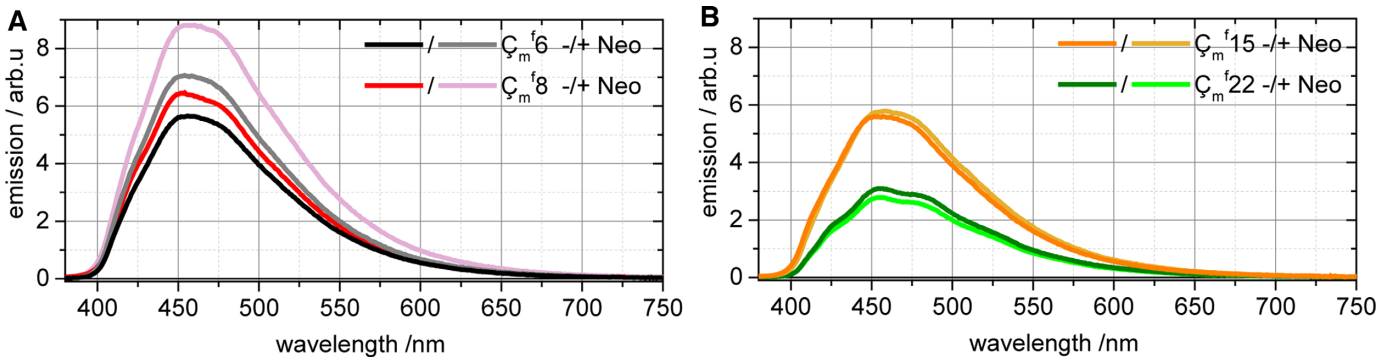

Figure 8. Concentration corrected steady-state emission spectra of (**A**) **Çm^{f}6**, **Çm^{f}8**, (**B**) **Çm^{f}15** and **Çm^{f}22** without (− **Neo**) and with neomycin (+ **Neo**).

pensation or superposition of effects the determination of T_{m-em} is more uncertain than the determination of T_{m-ab}.

The fluorescence-determined melting temperatures for the labeled aptamers range from 46°C to 59°C. The highest values were found for **Çm^{f}15** and **Çm^{f}22**, reflecting the high local stability of the stem and the terminal loop regions. On the other hand, the melting temperatures for **Çm^{f}6** and **Çm^{f}8**, placed in the internal loop, are significantly lower. This indicates that melting of the internal loop is the first stage in the unfolding of the aptamer. Furthermore, the higher melting temperatures of the ligand-bound state of **Çm^{f}6** and **Çm^{f}8** are consistent with stabilization of the folded internal loop by the ligand. On the other hand, the melting temperatures of **Çm^{f}15** and **Çm^{f}22** are slightly lower or not affected by the ligand. Thus, the binding of neomycin does not affect the stability of the terminal loop and the stem region.

Time resolved emission. The fluorescence lifetimes of the four fluorescently labeled aptamers differ slightly but sig-

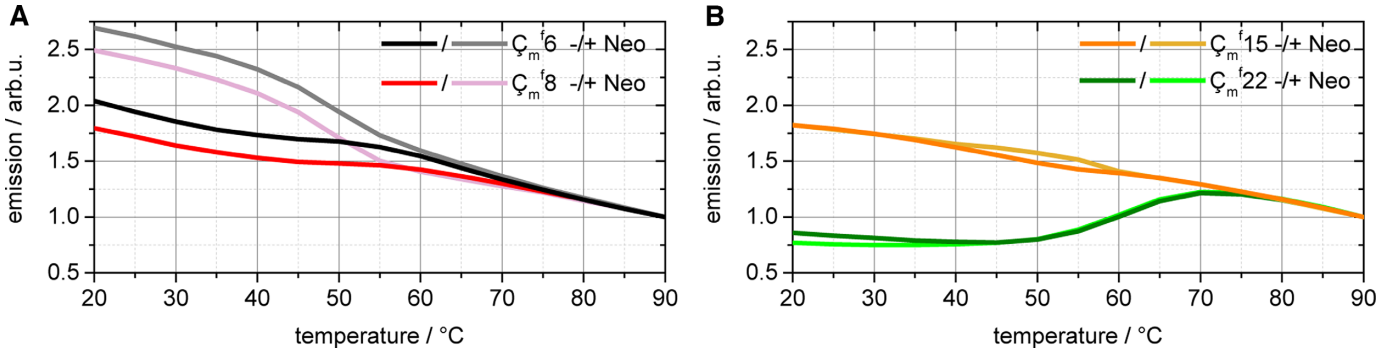

Figure 9. Melting curves of the **Çm^f** labeled neomycin aptamer without (−**Neo**) and with neomycin (+**Neo**) at 460 nm. The curves were normalized to the emission intensity at 90°C. (**A**) **Çm^{f}6**, **Çm^{f}8** (**B**) **Çm^{f}15**, **Çm^{f}22**.

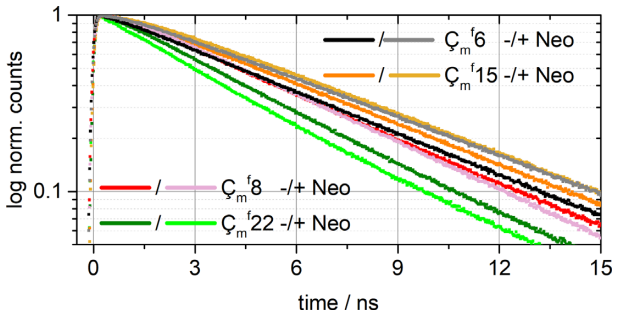

Figure 10. Normalized fluorescence decay of the different **Çm^f** labeled neomycin aptamer without (−**Neo**) and with neomycin (+**Neo**).

nificantly from each other (Figure 10 and Table 4). The average lifetimes in the absence of the neomycin ligand range from 4.6 to 5.4 ns, which is similar to what was observed for duplex RNA. Upon ligand binding, either a slight (5–10%) increase or decrease of the average fluorescence lifetime was observed, depending of the labeling position. This is a smaller difference in lifetimes than was observed between RNA single- and double-strands (ca. 40%). It is noteworthy that the fluorescence lifetimes of **Çm^{f}22** with and without neomycin are significantly shorter than the fluorescence lifetimes of the other samples, which indicates baseparing. This is in accord with the observed fine structure of the respective emission spectra for this sample and its fluorescence-monitored melting curves (Figure 9B).

Fluorescence stopped-flow. **Çm^{f}6** and **Çm^{f}8** were chosen for fluorescence stopped-flow measurements due to their large QY changes upon ligand binding (Figure 8A and Supplementary Figures S16–18). These experiments showed fast, ligand concentration-dependent binding kinetics; as the concentration of neomycin was raised, the binding rate increased (Figure 11). The increase in amplitude of the signal change leveled off after the addition of 4–6 equivalents neomycin.

The transients where analyzed with the DynaFit4 software. A one- and a two-step (with and without back reaction) as well as a Michaelis–Menten (70) model were tested (Table 5 and Supplementary Figures S16–18). The appropriate model was identified by the quality of the fit (RMSD) and the Akaike information criterion (ΔAIC) (71,72). It is evident from this analysis that the two-step model, in comparison to all other tested models, fits all the measured data by far the best (Tables 5–7 and Figure 11).

In the case of **Çm^{f}6**, the kinetics of the ligand-binding reaction can be described by a first reaction step with a bimolecular reaction rate constant of $k_1 = 425\ (\mu Ms)^{-1}$ and a second reaction step with a rate constant of $k_2 = 80\ s^{-1}$ (Figure 11A). The back-rates are significantly smaller than the corresponding rates of the forward reactions ($k_{-1} = 48\ s^{-1}$, $k_{-2} = 31\ s^{-1}$). Both reaction steps result in a fluorescence signal change of similar size (r(AL*) = 52%, r(AL) = 48%).

For **Çm^{f}8**, the first reaction rate constant was $k_1 = 207\ (\mu Ms)^{-1}$ and the second was $k_2 = 417\ s^{-1}$ (Figure 11A). As in the case of **Çm^{f}6**, the satisfactory fitting of both reaction steps requires the inclusion of back reactions. In this case the back-rates are significantly smaller ($k_{-1} = 113\ s^{-1}$, $k_{-2} = 125\ s^{-1}$) than the corresponding rates of the forward reactions. In contrast to **Çm^{f}6**, the first and the second reaction step of **Çm^{f}8** do not cause strong changes of the fluorescence signal. The signal response of the first reaction step is significantly weaker (r(AL*) = 22%) than the response of the second step (r(AL) = 78%).

In both labeled aptamer samples, **Çm^f** is a local probe for the micro-environment of the label. Because of the rigid incorporation of the label into the RNA, the nucleic acid itself dominates this micro-environment. Thus, local structural changes and local dynamics of the RNA can be monitored with the help of **Çm^f**. Therefore, the different dynamics of the two different **Çm^f**-labeled aptamers was expected.

Since sample heterogeneity is a common feature in complex biological systems, we tested our datasets for heterogeneity according to the described models. The datasets were fitted assuming two different aptamer species (A and B), which represent different aptamer structures. The increased number of fitting parameters would in fact improve the fits (data shown in the Supplementary Tables S17 and 18). Nevertheless, the fits yield unrealistic values and amplitudes which are subject to high errors. Furthermore, the converged fits always prefer one of the given species by more than 90%. Thus, we refrain to discuss a possible sample heterogeneity with quite complicated dynamics and concentrate on the analysis of the fit for a homogeneous sample, which should dominate the binding process of the aptamer.

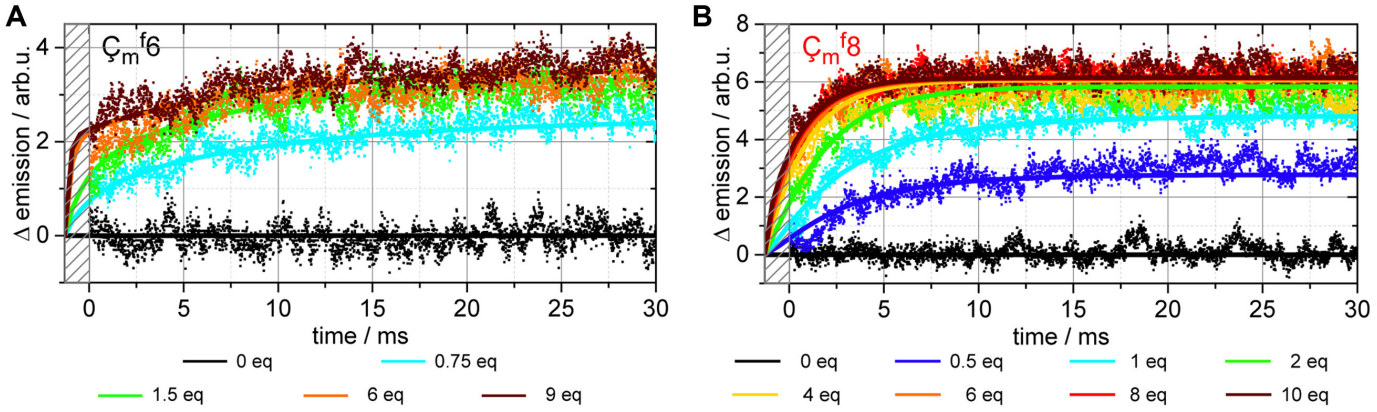

Figure 11. (**A**) Transient fluorescence signals after stopped-flow mixing of (**A**) 2.7 μM **Çm^{f}6** and (**B**) 4 μM **Çm^{f}8** with different concentrations of neomycin (indicated as equivalents of the aptamer concentration). The data are shown as points while the fits for a two-step model are displayed as solid lines.

Table 5. Reaction schemes of tested binding models

Model	Reaction scheme
One-step	$A + L \underset{k_{-1}}{\overset{k_1}{\rightleftharpoons}} AL$
Two-step (no back reaction)	$A + L \xrightarrow{k_1} AL^* \xrightarrow{k_2} AL$
Michaelis–Menten	$A + L \underset{k_{-1}}{\overset{k_1}{\rightleftharpoons}} AL^* \xrightarrow{k_2} AL$
Two-step	$A + L \underset{k_{-1}}{\overset{k_1}{\rightleftharpoons}} AL^* \underset{k_{-2}}{\overset{k_2}{\rightleftharpoons}} AL$

A = aptamer, L = ligand, AL* = ligand bound intermediate state, AL = final, ligand bound state, k_n = rate of reaction step n, k_{-n} = back-rate of reaction step n.

Table 6. Fit results of the tested binding models for the transient **Çm^{f}6** stopped-flow data

Model	$k_1/(\mu Ms)^{-1}$	k_{-1}/s^{-1}	k_2/s^{-1}	k_{-2}/s^{-1}	r(AL*)/%	r(AL)/%	RMSD	ΔAIC
One-step	131	3				100	0.0036	10 662
Two-step (no back reaction)	311		113		61	39	0.0029	1210
Michaelis-Menten	662	178	141		55	45	0.0028	387
Two-step	425	48	80	31	52	48	0.0028	0

k_n = rate of reaction step n, k_{-n} = back-rate of reaction step n, r(AL*) = signal response of component AL*, r(AL) = signal response of component AL, AIC = Akaike information criterion, RMSD = root-mean-square deviation.

Table 7. Fit results of the tested binding models for the transient Çm^{f}8 stopped-flow data

Model	$k_1/(\mu Ms)^{-1}$	k_{-1}/s^{-1}	k_2/s^{-1}	k_{-2}/s^{-1}	r(AL*)/%	r(AL)/%	RMSD	ΔAIC
One-step	92	6				100	0.0046	9194
Two-step (no back reaction)	120		637		44	56	0.0043	5228
Michaelis-Menten	141	100	609		44	56	0.0043	4956
Two-step	207	113	417	125	22	78	0.0040	0

k_n = rate of reaction step n, k_{-n} = back-rate of reaction step n, r(AL*) = signal response of component AL*, r(AL) = signal response of component AL, AIC = Akaike information criterion, RMSD = root-mean-square deviation.

DISCUSSION

Çm^f in single- and double-stranded RNA

Fluorescent labels provide unique insights into structural dynamics of RNA. Prior to a reliable analysis of aptamer conformation, a detailed characterization of the photophysical properties of the **Çm^f** fluorophore in model RNA was required. Altogether, the structural and photophysical properties (absorption and emission spectra; QY; fluorescence lifetime; structure; rigid incorporation into RNA; etc.) of **Çm^f** in RNA is very similar to the recently introduced fluorescent cytosine analog tC° (58) Nevertheless, **Çm^f** can be distinguished by several properties and details: the main difference between tC° and **Çm^f** is the quasi bifunctionality of **Çm^f**. As already described in the introduction, the fluorophore **Çm^f** is the isosteric precursor of the nitroxide spin-label **Çm**, which can be used for EPR studies on RNA. This

offers the possibility for highly comparable fluorescence and EPR studies on the same or very similar samples.

The emission spectra of **Ç$_m^f$** did not change significantly upon incorporation into RNA single-strands, although and in contrast to tC° the QY as well as the fluorescence lifetime of the fluorophore increased notably. As we have previously shown, both values of **Ç$_m^f$** are strongly affected by solvent interactions (68). Therefore, the shielding of the chromophore against quenching solvent interactions, the stabilization of its S_1 state and consequently the decrease of the non-radiative decay rate is a likely explanation for the higher QY and the longer fluorescence lifetime of **C$_m^f$** in RNA single-strands. The enhanced shielding might be due to steric effects of the neighboring nucleobases as well as base-stacking interactions. This would also provide a consistent explanation for the higher QY in the case of neighboring purine bases, which are expected to stack better.

Incorporation of **Ç$_m^f$** into RNA duplexes, on the other hand, leads to a lower QY and to a fine structured emission spectrum. Both effects are much more pronounced for **Ç$_m^f$** than for tC° (58). Gardarsson *et al*. have shown that deprotonation at the N5 position of **Ç^f** or weakening of the N-H-bond decreases the QY of the chromophore and leads to a similarly structured emission spectrum (54). Therefore, it is possible that formation of a hydrogen bond between **Ç$_m^f$** and guanine in a base pair destabilizes the S_1 state, which would counteract and overcompensate the stabilizing effects of steric shielding and base stacking. The significant changes in the spectral shape of the emission spectra and the large changes of the QY upon duplex formation of **Ç$_m^f$**-labeled RNA oligonucleotides make **Ç$_m^f$** a sensitive probe of its micro-environment.

Thermal denaturation experiments of the **Ç$_m^f$**-labeled duplexes were performed to evaluate whether **Ç$_m^f$** caused any structural perturbations. These experiments were monitored by two different methods: the absorption change at 260 nm yields the global melting temperature and detection of the **Ç$_m^f$** emission at 460 nm provides information on the melting transition in the vicinity of the label (Table 3 and Figure 4). The similar T_m-values obtained in global and local melting assays support the assumption that the double-strands melt uniformly. The small T_m-differences between the labeled and unlabeled duplexes (3°C or less, ΔG 0–5 kcal/mol) indicate that **Ç$_m^f$**, like tC°, has no appreciable effect on RNA duplex stability. The increased T_m of ds_C**Ç$_m^f$**C and ds_G**Ç$_m^f$**G compared to ds_U**Ç$_m^f$**U and ds_A**Ç$_m^f$**A are simply due to higher CG content.

Interestingly, we observed fine-structure in the emission spectra of **Ç$_m^f$** in RNA, but, in contrast to tC°, only when base-paired. This provided an opportunity to extract more information from the thermal denaturation data, using what we refer to as spectrally resolved melting analysis, which allows probing of the local melting process. This evaluation yields the temperature where half of the sample appears to be base paired at the position of the label. This temperature was found to be significantly lower than the melting temperatures of the RNA duplexes and might identify an early step in the overall melting process.

The significant anisotropy differences between the free label in solution, labeled single-strands and labeled double-strands further substantiate the rigid incorporation of **Ç$_m^f$** in RNA. The slight variation of the anisotropy values with the neighboring bases of the label might be due to the different fluorescence lifetimes of the fluorophore in the different RNA strands. This can be explained with the (anti-)correlation of these properties (cf. Perrin equation (73)).

Ç$_m^f$-labeled neomycin aptamers

The experiments for the model strands demonstrate that the steady-state emission signal of **Ç$_m^f$** is an excellent probe for the micro-environment of the label. The QY of **Ç$_m^f$** depends on the labeling position and responds in a characteristic way to ligand interaction or binding. ITC measurements indicate, that neomycin is specifically bound by **Ç$_m^f$6**, **Ç$_m^f$8** and **Ç$_m^f$15**, while there is no efficient neomycin binding by **Ç$_m^f$22**. The considerably increased K_Ds of **Ç$_m^f$6**, **Ç$_m^f$8** and **Ç$_m^f$15** in comparison to the unlabeled aptamer might be due to the positively charged **Ç$_m^f$** at pH 7.4, which could reduce the affinity of the protonated neomycin electrostatically.

Despite the finding that **Ç$_m^f$22** does not bind the ligand specifically, the QY of **Ç$_m^f$22** is reduced in the presence of the ligand. This might be due to unspecific interactions between the label and the ligand, which also lead to a noticeable destabilization of the labeled aptamer within the absorption monitored thermal denaturation experiments. The fine structure of the **Ç$_m^f$22** emission as well as the strong fluorescence quenching found in the emission monitored thermal denaturation experiments are both due to hydrogen bonds between **Ç$_m^f$** and the complementary guanosine. This effect is independent of the presence of the ligand. Thus, at least a significant amount of **Ç$_m^f$22** has to be base paired at the labeling position.

The fluorescence signals of **Ç$_m^f$15** are not affected by the addition of neomycin at all and only very weak signal changes are observable within the thermal denaturation experiments. It can thus be concluded, that the micro-environment of **Ç$_m^f$** at position 15 does not change upon ligand binding, which meets our expectations for this reference aptamer, since position 15 is not directly involved in the formation of the binding pocket (Figure 7). The strongest changes in the emission can be seen for **Ç$_m^f$6** and **Ç$_m^f$8**, which is indicative for direct interactions between ligand and label as well as larger structural changes of the aptamer in the label region. This is in agreement with a direct involvement of these residues in ligand binding (Figure 7).

In comparison with the unlabeled neomycin aptamer, absorption monitored melting experiments show that the fluorescence labeling does not critically destabilize the aptamers **Ç$_m^f$6** and **Ç$_m^f$8** in the ligand-free state. In the ligand-bound state a destabilization, in comparison with the unlabeled neomycin aptamer, is noticeable. Fluorescence monitored melting curves provide further site-specific information on the interactions between label, ligand and aptamer: the fold without ligand of **Ç$_m^f$6** and **Ç$_m^f$8** results in a slight quenching of the fluorophore. In the presence of the ligand the QY of **Ç$_m^f$6** and **Ç$_m^f$8** increases, the fluorescence quenching is thus overcompensated, indicating a different fold of the aptamer at the labeled positions or direct interactions between label and ligand.

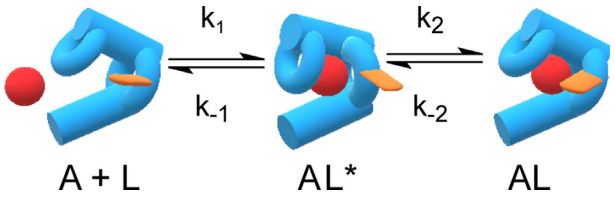

Figure 12. Cartoon of the proposed two-step binding model. The ligand is depicted as red sphere, the label as orange plate and the aptamer as blue clamp. A = aptamer, L = ligand, AL* = ligand bound intermediate state, AL = final, ligand bound state, k_n = rate of reaction step n, k_{-n} = back-rate of reaction step n.

Generally, with the help of the fluorescence monitored melting experiments stabilization and destabilization effects due to ligand binding can be observed and discussed on a local level. A detailed explanation of these effects in different regions of the tertiary structure of the aptamer is not straightforward with the current dataset. Nevertheless, these relatively weak stability changes provide evidence for at least small conformational changes upon ligand binding.

To test this conclusion, the steady-state fluorescence anisotropy was measured: based on the assumption, that at all labeling positions the chromophore is rigidly incorporated into the neomycin aptamer, it is possible to conceptually connect the fluorescence anisotropy to the volume of the aptamer. Consequently, it seems as if the volume and the shape of the neomycin aptamer does not change significantly upon ligand binding. In the case of extended tertiary structural changes, one would expect a stronger change of the anisotropy. Thus, the more or less constant fluorescence anisotropy value confirms the preformation of the aptamer and the conformational selection binding mechanism. Nevertheless, small conformational changes, which do not significantly change the shape of the aptamer, cannot be ruled out via fluorescence anisotropy methods.

In accordance to the low sub-μM K_Ds of the $\mathbf{Ç_m^f 6}$ and $\mathbf{Ç_m^f 8}$ labeled aptamers, the stopped-flow measurements show very rapid binding dynamics. It becomes apparent, that a two-step binding model—with a back and forward reaction for each step—describes the data best. Based on these findings it is possible to propose the following binding mechanism of the neomycin aptamer (Figure 12): the aptamer is mostly preformed in solution (pH 7.4, 20°C). In a first step, neomycin enters the preformed binding pocket of the aptamer. Unspecific interactions between ligand and fluorescent label cause an increase of the emission signal. In a second step, specific interactions, like hydrogen bonds and electrostatic interactions, between the ligand and the binding pocket are formed. This induces small conformational changes in the area of the binding pocket. Thus, the overall shape of the aptamer is not distorted but the microenvironment (orientation, solvent accessibility) of the fluorescent label is modified. This affects the non-radiative de-excitation rate of the label and also results in an increased QY.

CONCLUSION

This study presents the features and the potential of $\mathbf{Ç_m^f}$ as a fluorescent RNA label. A 5′-dimethoxytritylated phosphoramidite was synthesized from the fluorescent nucleoside $\mathbf{Ç_m^f}$ (45), which was then incorporated into RNA via solid-phase oligonucleotide synthesis.

The stability of the duplexes was not affected by insertion of the fluorescent label. As with DNA the emission spectra become structured upon duplex formation. As the QY is affected by the flanking bases of the fluorophore, it was possible to distinguish between pyrimidine and purine neighboring bases. Fluorescence lifetime measurements allowed distinguishing between labeled double- and single-strands and also between flanking bases of the fluorophore. The $\mathbf{Ç_m^f}$-fluorophore is sensitive to its micro-environment such as base pairing, stacking and solvent accessibility. Thus, specific $\mathbf{Ç_m^f}$-labeled RNA samples are perfectly suitable for duplexation and ligand binding studies. Time resolved fluorescence measurements of $\mathbf{Ç_m^f}$-labeled samples allow structural dynamics studies. Our results can thus serve as benchmarks for analogous experiments on functional RNAs for example aptamers.

Subsequently, a ligand binding study of the neomycin aptamer was performed. The aptamer was singly labeled at four different positions. With steady-state fluorescence methods, it was possible to confirm the previously proposed conformational selection mechanism, with a widely preformed aptamer, as binding model for the neomycin aptamer. Moreover, it was possible to observe the dynamics of the ligand binding process with the help of fluorescence-monitored stopped-flow measurements. It comes clear that the ligand binding is in fact a two-step process. We propose an unspecific ligand binding near or in the binding pocket as a first step. In the second step, the ligand is bound specifically with the help of H-bonds and electrostatic interactions. It is proposed, that this second step causes only minor conformational changes.

In general, our results open the door for further RNA binding studies with $\mathbf{Ç_m^f}$. In the case of the neomycin aptamer further pH- or salt-concentration-dependent studies as well as studies with other label positions are conceivable. $\mathbf{C_m^f}$ in combination with other RNA-labels should enable FRET measurements. These would allow a direct comparison between UV/vis and PELDOR data. Furthermore, the presented results provide evidence for a kinetic contribution to the regulatory mechanism of the neomycin aptamer. In comparison and in combination with other studies on dynamics and structure this might help to understand the regulatory mechanisms of riboswitches in greater detail.

DATA AVAILABILITY

OPTIMUS is free for academic use and available under http://optimusfit.org.

DynaFit 4 is free for academic use and available under http://www.biokin.com/dynafit.

SEDPHAT is free for academic use and available under http://www.analyticalultracentrifugation.com/sedphat/.

NITPIC is free for academic use and available under http://biophysics.swmed.edu/MBR/software.html.

SUPPLEMENTARY DATA

Supplementary Data are available at NAR Online.

ACKNOWLEDGEMENTS

We thank L. Tapmeyer, A. Völklein, J. Martin and M. Kuth for their support regarding several steady-state and time resolved absorption and fluorescence measurements. We thank Prof. A. Heckel for access to his absorption spectrometer with sample changer. We thank Prof. J. Wöhnert for access to his ITC. Furthermore, we thank Dr M. Vogel and Prof. B. Süß for fruitful discussions concerning the neomycin aptamer.

FUNDING

Deutsche Forschungsgemeinschaft (DFG) through the Collaborative Research Center (CRC) 902; 'Molecular Principles of RNA-based Regulation' sub-projects A7, B14 and Mercator Fellowship. Funding for open access charge: DFG (CRC902); sub-projects A7, B14 and Mercator Fellowship.

Conflict of interest statement. None declared.

REFERENCES

1. Altman,S. (1990) Enzymatic cleavage of RNA by RNA (Nobel lecture). *Angew. Chem. Int. Ed. Engl.*, **29**, 749–758.
2. Cech,T.R. (1990) Self-splicing and enzymatic activity of an intervening sequence RNA from Tetrahymena (Nobel Lecture). *Biosci. Rep.*, **10**, 239–261.
3. Gilbert,W. (1986) Origin of life: the RNA world. *Nature*, **319**, 618.
4. Robertson,M.P. and Joyce,G.F. (2012) The origins of the RNA world. *Cold Spring Harb. Perspect. Biol.*, **4**, a003608.
5. Morris,K. V. and Mattick,J.S. (2014) The rise of regulatory RNA. *Nat. Rev. Genet.*, **15**, 423–437.
6. Cech,T.R. and Steitz,J.A. (2014) The noncoding RNA revolution—trashing old rules to forge new ones. *Cell*, **157**, 77–94.
7. Serganov,A. and Nudler,E. (2013) A decade of riboswitches. *Cell*, **152**, 17–24.
8. Chen,X., Li,N. and Ellington,A.D. (2007) Ribozyme catalysis of metabolism in the RNA world. *Chem. Biodivers.*, **4**, 633–655.
9. Breaker,R.R. (2012) Riboswitches and the RNA world. *Cold Spring Harb. Perspect. Biol.*, **4**, a003566.
10. Breaker,R.R. (2009) Riboswitches: from ancient gene-control systems to modern drug targets. *Future Microbiol.*, **4**, 771–773.
11. Garst,A.D., Edwards,A.L. and Batey,R.T. (2011) Riboswitches: structures and mechanisms. *Cold Spring Harb. Perspect. Biol.*, **3**, a003533.
12. Batey,R.T. (2015) Riboswitches: still a lot of undiscovered country. *RNA*, **21**, 560–563.
13. Weigand,J.E., Sanchez,M., Gunnesch,E.-B.E.-B., Zeiher,S., Schroeder,R. and Suess,B. (2008) Screening for engineered neomycin riboswitches that control translation initiation. *RNA*, **14**, 89–97.
14. Berens,C., Groher,F. and Suess,B. (2015) RNA aptamers as genetic control devices: The potential of riboswitches as synthetic elements for regulating gene expression. *Biotechnol. J.*, **10**, 246–257.
15. Weigand,J.E. and Suess,B. (2009) Aptamers and riboswitches: perspectives in biotechnology. *Appl. Microbiol. Biotechnol.*, **85**, 229–236.
16. Ellington,A.D. and Szostak,J.W. (1990) In vitro selection of RNA molecules that bind specific ligands. *Nature*, **346**, 818–822.
17. Tuerk,C. and Gold,L. (1990) Systematic evolution of ligands by exponential enrichment: RNA ligands to bacteriophage T4 DNA polymerase. *Science*, **249**, 505–510.
18. Robertson,D.L. and Joyce,G.F. (1990) Selection in vitro of an RNA enzyme that specifically cleaves single-stranded DNA. *Nature*, **344**, 467–468.
19. Duchardt-Ferner,E., Gottstein-Schmidtke,S.R., Weigand,J.E., Ohlenschläger,O., Wurm,J.-P., Hammann,C., Suess,B. and Wöhnert,J. (2016) What a difference an OH makes: Conformational dynamics as the basis for the ligand specificity of the neomycin-sensing riboswitch. *Angew. Chem. Int. Ed.*, **55**, 1527–1530.
20. Duchardt-Ferner,E., Weigand,J.E., Ohlenschläger,O., Schmidtke,S.R., Suess,B. and Wöhnert,J. (2010) Highly modular structure and ligand binding by conformational capture in a minimalistic riboswitch. *Angew. Chem. Int. Ed.*, **49**, 6216–6219.
21. Krstić,I., Frolow,O., Sezer,D., Endeward,B., Weigand,J.E., Suess,B., Engels,J.W. and Prisner,T.F. (2010) PELDOR spectroscopy reveals preorganization of the neomycin-responsive riboswitch tertiary structure. *J. Am. Chem. Soc.*, **132**, 1454–1455.
22. Perez-Gonzalez,C., Lafontaine,D.A. and Penedo,J.C. (2016) Fluorescence-based strategies to investigate the structure and dynamics of aptamer-ligand complexes. *Front. Chem.*, **4**, 1–22.
23. Ward,D.C. and Reich,E. (1969) Studies of nucleotides and polynucleotide. *J. Biochem. Chem.*, **244**, 1228–1237.
24. Jean,J.M. and Hall,K.B. (2001) 2-Aminopurine fluorescence quenching and lifetimes: Role of base stacking. *Proc. Natl. Acad. Sci. U.S.A.*, **98**, 37–41.
25. Jones,A.C. and Neely,R.K. (2015) 2-aminopurine as a fluorescent probe of DNA conformation and the DNA-enzyme interface. *Q. Rev. Biophys.*, **48**, 244–279.
26. Rist,M.J. and Marino,J.P. (2002) Fluorescent nucleotide base analogs as probes of nucleic acid structure, dynamics and interactions. *Curr. Org. Chem.*, **6**, 775–793.
27. Matarazzo,A. and Hudson,R.H.E. (2015) Fluorescent adenosine analogs: a comprehensive survey. *Tetrahedron*, **71**, 1627–1657.
28. Reuss,A.J., Grünewald,C., Gustmann,H., Engels,J.W. and Wachtveitl,J. (2017) Three-state fluorescence of a 2-functionalized pyrene-based RNA label. *J. Phys. Chem. B*, **121**, 3032–3041.
29. Förster,U., Lommel,K., Sauter,D., Grünewald,C., Engels,J.W. and Wachtveitl,J. (2010) 2-(1-ethynylpyrene)-adenosine as a folding probe for RNA—pyrene in or out. *Chembiochem*, **11**, 664–672.
30. Förster,U., Grünewald,C., Engels,J.W. and Wachtveitl,J. (2010) Ultrafast dynamics of 1-ethynylpyrene-modified RNA: A photophysical probe of intercalation. *J. Phys. Chem. B*, **114**, 11638–11645.
31. Förster,U., Gildenhoff,N., Grünewald,C., Engels,J.W. and Wachtveitl,J. (2009) Photophysics of 1-ethynylpyrene-modified RNA base adenine. *J. Lumin.*, **129**, 1454–1458.
32. Grünewald,C., Kwon,T., Piton,N., Förster,U., Wachtveitl,J. and Engels,J.W. (2008) RNA as scaffold for pyrene excited complexes. *Bioorg. Med. Chem.*, **16**, 19–26.
33. Rovira,A.R., Fin,A. and Tor,Y. (2015) Chemical mutagenesis of an emissive RNA alphabet. *J. Am. Chem. Soc.*, **137**, 14602–14605.
34. Sandin,P., Wilhelmsson,L.M., Lincoln,P., Powers,V.E.C., Brown,T. and Albinsson,B. (2005) Fluorescent properties of DNA base analogue tC upon incorporation into DNA - Negligible influence of neighbouring bases on fluorescence quantum yield. *Nucleic Acids Res.*, **33**, 5019–5025.
35. Shin,D., Sinkeldam,R.W. and Tor,Y. (2011) Emissive RNA alphabet. *J. Am. Chem. Soc.*, **133**, 14912–14915.
36. Wojciechowski,F. and Hudson,R.H.E. (2008) Fluorescence and hybridization properties of peptide nucleic acid containing a substituted phenylpyrrolocytosine designed to engage guanine with an additional H-Bond. *J. Am. Chem. Soc.*, **130**, 12574–12575.
37. Wilhelmsson,L.M. and Tor,Y. (2010) Fluorescent analogs of biomolecular building blocks: Design and applications. *Chem. Rev.*, **110**, 2579–2619.
38. Wilhelmsson,L.M. (2010) Fluorescent nucleic acid base analogues. *Q. Rev. Biophys.*, **43**, 159–183.
39. Trojanowski,P., Plötner,J., Grünewald,C., Graupner,F.F., Slavov,C., Reuss,A.J., Braun,M., Engels,J.W. and Wachtveitl,J. (2014) Photo-physical properties of 2-(1-ethynylpyrene)-adenosine: influence of hydrogen bonding on excited state properties. *Phys. Chem. Chem. Phys.*, **16**, 13875–13888.
40. Reuss,A.J., Grünewald,C., Braun,M., Engels,J.W. and Wachtveitl,J. (2016) The three possible 2- (pyrenylethynyl) adenosines: Rotameric energy barriers govern the photodynamics of these structural isomers. *Chemphyschem*, **17**, 1369–1376.
41. Barhate,N., Cekan,P., Massey,A.P.P. and Sigurdsson,S.T.T. (2007) A nucleoside that contains a rigid nitroxide spin label: A fluorophore in disguise. *Angew. Chem. Int. Ed. Engl.*, **46**, 2655–2658.
42. Marko,A., Denysenkov,V., Margraf,D., Cekan,P., Schiemann,O., Sigurdsson,S.T. and Prisner,T.F. (2011) Conformational flexibility of DNA. *J. Am. Chem. Soc.*, **133**, 13375–13379.

43. Cekan,P., Jonsson,E.O. and Sigurdsson,S.T. (2009) Folding of the cocaine aptamer studied by EPR and fluorescence spectroscopies using the bifunctional spectroscopic probe Ç. *Nucleic Acids Res.*, **37**, 3990–3995.
44. Shelke,S.A., Sandholt,G.B. and Sigurdsson,S.T. (2014) Nitroxide-labeled pyrimidines for non-covalent spin-labeling of abasic sites in DNA and RNA duplexes. *Org. Biomol. Chem.*, **12**, 7366–7374.
45. Höbartner,C., Sicoli,G., Wachowius,F., Gophane,D.B. and Sigurdsson,S.T. (2012) Synthesis and characterization of RNA containing a rigid and nonperturbing cytidine-derived spin label. *J. Org. Chem.*, **77**, 7749–7754.
46. Cekan,P. and Sigurdsson,S.T. (2008) Single base interrogation by a fluorescent nucleotide: each of the four DNA bases identified by fluorescence spectroscopy. *Chem. Commun.*, **0**, 3393–3395.
47. Schiemann,O., Cekan,P., Margraf,D., Prisner,T.F. and Sigurdsson,S.T. (2009) Relative orientation of rigid nitroxides by PELDOR: Beyond distance measurements in nucleic acids. *Angew. Chem. Int. Ed. Engl.*, **48**, 3292–3295.
48. Edwards,T.E., Cekan,P., Reginsson,G.W., Shelke,S. a, Ferré-D'Amaré,A.R., Schiemann,O. and Sigurdsson,S.T. (2011) Crystal structure of a DNA containing the planar, phenoxazine-derived bi-functional spectroscopic probe Ç. *Nucleic Acids Res.*, **39**, 4419–4426.
49. Prisner,T.F., Marko,A. and Sigurdsson,S.T. (2015) Conformational dynamics of nucleic acid molecules studied by PELDOR spectroscopy with rigid spin labels. *J. Magn. Reson.*, **252**, 187–198.
50. Grytz,C.M., Marko,A., Cekan,P., Sigurdsson,S.T. and Prisner,T.F. (2016) Flexibility and conformation of the cocaine aptamer studied by PELDOR. *Phys. Chem. Chem. Phys.*, **18**, 2993–3002.
51. Likhtenshtein,G.I., Yamauchi,J., Nakatsuji,S., Smirnov,A.I. and Tamura,R. (2008) *Nitroxides: Applications in Chemistry, Biomedicine, and Materials Science*, WILEY-VCH Verlag GmbH & Co. KGaA, Weinheim.
52. Likhtenstein,G.I., Ishii,K. and Nakatsuji,S. (2007) Dual chromophore-nitroxides: Novel molecular probes photochemical and photophysical models and magnetic materials. *Photochem. Photobiol.*, **83**, 871–881.
53. Stryer,L. and Griffith,O.H. (1965) A spin-labeled hapten. *Proc. Natl. Acad. Sci. U.S.A.*, **54**, 1785–1791.
54. Gardarsson,H., Kale,A.S. and Sigurdsson,S.T. (2011) Structure-function relationships of phenoxazine nucleosides for identification of mismatches in duplex DNA by fluorescence spectroscopy. *Chembiochem*, **12**, 567–575.
55. Cekan,P. and Sigurdsson,S.T. (2012) Conformation and dynamics of nucleotides in bulges and symmetric internal loops in duplex DNA studied by EPR and fluorescence spectroscopies. *Biochem. Biophys. Res. Commun.*, **420**, 656–661.
56. Gardarsson,H. and Sigurdsson,S.T. (2010) Large flanking sequence effects in single nucleotide mismatch detection using fluorescent nucleoside Çf. *Bioorg. Med. Chem.*, **18**, 6121–6126.
57. Tkach,I., Pornsuwan,S., Höbartner,C., Wachowius,F., Sigurdsson,S.T., Baranova,T.Y., Diederichsen,U., Sicoli,G. and Bennati,M. (2013) Orientation selection in distance measurements between nitroxide spin labels at 94 GHz EPR with variable dual frequency irradiation. *Phys. Chem. Chem. Phys.*, **15**, 3433–3437.
58. Füchtbauer,A.F., Preus,S., Börjesson,K., McPhee,S.A., Lilley,D.M.J. and Wilhelmsson,L.M. (2017) Fluorescent RNA cytosine analogue—an internal probe for detailed structure and dynamics investigations. *Sci. Rep.*, **7**, 2393.
59. Mergny,J.-L. and Lacroix,L. (2003) Analysis of thermal melting curves. *Oligonucleotides*, **13**, 515–537.
60. Weigand,J.E., Gottstein-Schmidtke,S.R., Demolli,S., Groher,F., Duchardt-Ferner,E., Wöhnert,J. and Suess,B. (2014) Sequence elements distal to the ligand binding pocket modulate the efficiency of a synthetic riboswitch. *Chembiochem*, **15**, 1627–1637.
61. Keller,S., Vargas,C., Zhao,H., Piszczek,G., Brautigam,C.A. and Schuck,P. (2012) High-precision isothermal titration calorimetry with automated peak-shape analysis. *Anal. Chem.*, **84**, 5066–5073.
62. Scheuermann,T.H. and Brautigam,C.A. (2015) High-precision, automated integration of multiple isothermal titration calorimetric thermograms: New features of NITPIC. *Methods*, **76**, 87–98.
63. Zhao,H., Piszczek,G. and Schuck,P. (2015) SEDPHAT—a platform for global ITC analysis and global multi-method analysis of molecular interactions. *Methods*, **76**, 137–148.
64. Enderlein,J. and Erdmann,R. (1997) Fast fitting of multi-exponential decay curves. *Opt. Commun.*, **134**, 371–378.
65. Berger,R.L. and Friauf,B.B.B. (1968) High speed optical stopped-flow apparatus high speed optical stopped-flow apparatus. *Rev. Sci. Instrum.*, **39**, 486–493.
66. Berger,R.L., Balko,B. and Chapman,H.F. (1968) High resolution mixer for the study of the kinetics of rapid reactions in solution. *Rev. Sci. Instrum.*, **39**, 493–498.
67. Kuzmic,P. (1996) Program DYNAFIT for the analysis of enzyme kinetic data: application to HIV proteinase. *Anal. Biochem.*, **273**, 260–273.
68. Gustmann,H., Lefrancois,D., Reuss,A.J., Gophane,D.B., Braun,M., Dreuw,A., Sigurdsson,S.T. and Wachtveitl,J. (2017) Spin the light off: rapid internal conversion into a dark doublet state quenches the fluorescence of an RNA spin label. *Phys. Chem. Chem. Phys.*, **19**, 26255–26264.
69. Weigand,J.E., Schmidtke,S.R., Will,T.J., Duchardt-Ferner,E., Hammann,C., Wöhnert,J., Suess,B., Wohnert,J. and Suess,B. (2011) Mechanistic insights into an engineered riboswitch: a switching element which confers riboswitch activity. *Nucleic Acids Res.*, **39**, 3363–3372.
70. Johnson,K.A. and Goody,R.S. (2011) The original Michaelis constant: translation of the 1913 Michaelis − Menten paper. *Biochemistry*, **50**, 8264–8269.
71. Akaike,H. (1974) A new look at the statistical model identification. *IEEE Trans. Autom. Control*, **19**, 716–723.
72. Myung,J., Tang,Y. and Pitt,M.A. (2009) Evaluation and comparison of computational models. *Methods Enzymol.*, **454**, 287–304.
73. Lakowicz,J.R. (2006) *Principles of Fluorescence Spectroscopy*. 3rd edn. Springer Science+Business Media, LCC, NY.